Figure 17.8 A set of images taken with a 320 × 256 format LWIR CBIRD FPA operating at 78 K.

differential temperature (NEΔT) values of 18.6 mK and 12 mK operating at 78 K and 65 K, respectively. The mean specific detectivity of $D^* = 1.3 \times 10^{11}$ cm-Hz$^{1/2}$/W was found for 78K operating temperature. Figure 17.8 shows several images taken with this FPA at an operating temperature of 78 K. Other system-level performance metrics such as minimum resolvable temperature difference (MRΔT) and modulation transfer function (MTF) have also been measured. A detailed account of the FPA performance can be found in Ref. 54.

17.3 Quantum-Dot Barrier Infrared Detector (QD-BIRD)

The recent emergence of BIRDs such as the nBn[3] and the XBn[6] have resulted in MWIR detectors with substantially higher operating temperatures than previously available in III-V-semiconductor-based MWIR detectors. The initial nBn devices used either InAs absorber grown on InAs substrate, or lattice-matched InAsSb alloy grown on GaSb substrate, with cutoff wavelengths of $\sim$3.2 μm and $\sim$ 4 μm, respectively. While these detectors could operate at much higher temperatures than existing MWIR detectors based on InSb, their spectral responses do not cover the full (3–5 μm) MWIR atmospheric transmission window. This has led to the development of nBn detectors such as those based on the InAs/GaSb type-II SL (T2SL) absorber.[11,55] In this section, we describe our effort in combining the unipolar BIRD device architecture with alternative infrared absorbers based on InSb QDs embedded in an InAsSb matrix in order to achieve extended spectral coverage.[18]

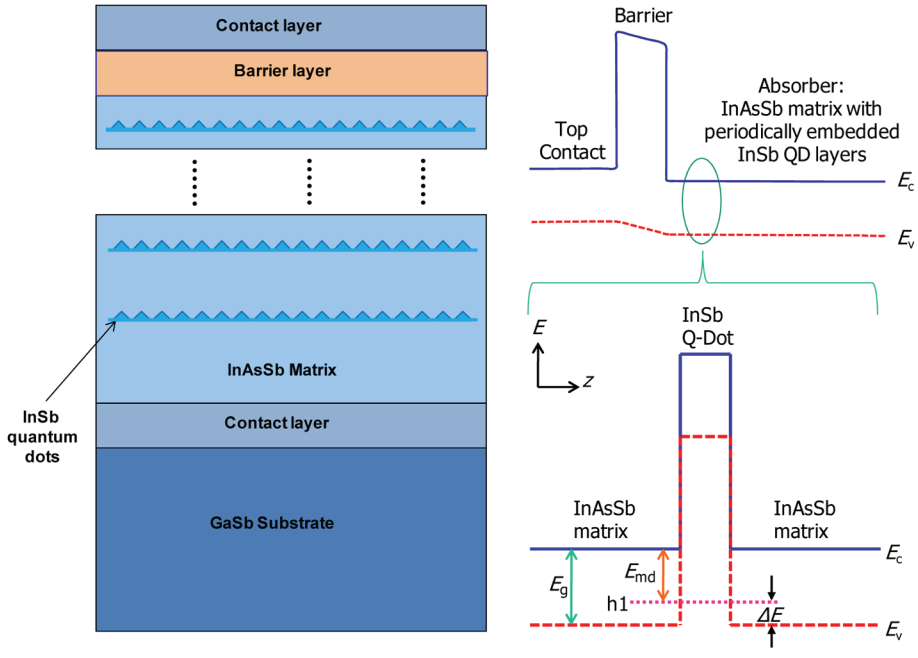

Figure 17.9 (a) Schematic layer diagram of the QD-BIRD structure. (b) (Top) Schematic energy band diagram of the active region of the QD-BIRD device; (bottom) expanded view of the schematic energy band diagram for the QD-BIRD absorber near an InSb quantum-dot layer.

The schematic layer diagram in Fig. 17.9 shows the growth sequence of the QD-BIRD. The energy band diagram illustrates the structure of the QD-BIRD, which is very similar to the standard nBn device structure as originally described by Maimon and Wicks,[3] consisting of an AlSbAs barrier sandwiched between the InAsSb top contact layer and absorber layer. The slight modification we introduced is the periodic insertion of 2.8 monolayers (MLs) of InSb, which form self-assembled InSb QD layers in the InAsSb absorber matrix, as illustrated in Fig. 17.9. The alloy composition of the InAsSb matrix was adjusted slightly to reduce the Sb content. Details of the structure have been reported earlier.[18]

Figure 17.10 shows the normalized PL spectrum of the QD-BIRD with two distinct peaks at 4.0 μm and 5.5 μm. The origins of the two peaks are illustrated in the bottom right panel of Fig. 17.9, which shows the schematic energy band diagram in the vicinity of an InSb quantum-dot insertion layer in the InAsSb matrix. The 4.0-μm peak is easily identified with the bandgap E_g of the InAsSb matrix. The 5.5-μm peak is related to the QD. The band diagram shows that the strained InSb forms a type-II broken-gap band alignment with the InAsSb matrix, with both the conduction- and valence-band edge of InSb being substantially higher than the conduction-band edge of InAsSb. The InSb

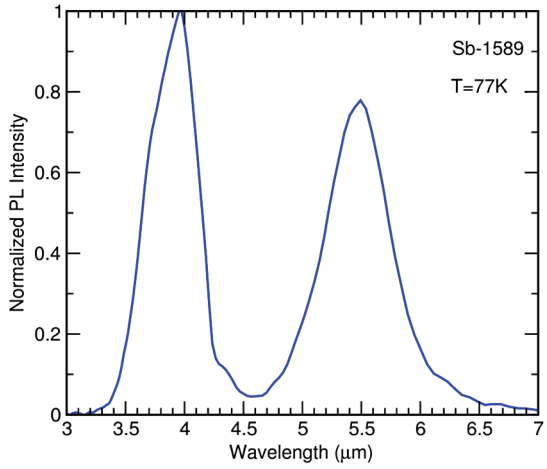

Figure 17.10 PL spectrum for the QD-BIRD taken at $T = 77$ K.

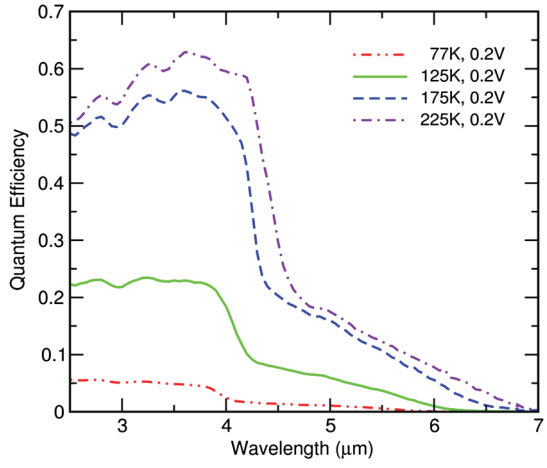

Figure 17.11 Multipass spectral QE of a QD-BIRD without AR coating under −0.2-V applied bias, measured at 77, 125, 175, and 225 K. (See color plate section.)

quantum-dot conduction-band state is clearly unconfined and is therefore not a likely source of the PL peak. What is most probably responsible for the 5.5-μm PL peak is a type-II transition involving the conduction-band edge of the InAsSb matrix, and the confined hole state of the InSb QD. This transition is illustrated in the bottom of Fig. 17.9(b) and is labeled E_{md}.

Figure 17.11 shows the spectral QE for a QD-BIRD device, without AR coating, taken at 77, 125, 175, and 225 K under −200-mV bias. The spectral response is measured using a top-illuminated geometry. Because the GaSb substrate is essentially transparent to the MWIR radiation under consideration, the spectral response should be considered as a double-pass (or multiple-pass)

result, since after initially passing through the absorber, light could re-enter the absorber region after reflecting off the bottom of the substrate (the test devices are mounted on a chip carrier with a metallic surface). Like the PL spectrum, the spectral QE also shows a distinct bimodal behavior. The photoresponse associated with the direct band-to-band transition in the InAsSb matrix is seen at the shorter wavelengths, with approximate plateau QE values of 0.055, 0.33, 0.55, and 0.61 at $T = 77$, 125, 175, and 225 K, respectively. For this InAsSb matrix response, the 50% QE cutoff wavelengths are approximately 3.97, 4.15, 4.30, and 4.46 μm at $T = 125$, 175, and 225 K, respectively.

Beyond the cutoff wavelength associated with the bulk InAsSb matrix, we also observe an extended response that drops off approximately linearly; this is attributed to the type-II transition between the QD valence-band state and the InAsSb matrix conduction-band state. The extended response associated with the QDs is noticeably weaker than the bulk InAsSb response. The external quantum efficiencies at 5 μm for $T = 77$, 125, 175, and 225 K are respectively 0.011, 0.086, 0.16, and 0.175, which are only approximately 20–30% of the corresponding values found for the InAsSb matrix in the 3- to 4-μm range, even though the PL intensities of the QD-to-matrix and the bulk transitions are comparable. One possible reason for the weaker response of the QD-to-matrix transition is that the QD hole state is confined by the InAsSb matrix. The confinement energy ΔE is given by the difference between the InAsSb bandgap E_g and the QD-to-matrix transition energy E_{md} (see Fig. 17.9). The photoexcited hole (minority carrier) in the QD has to overcome this additional energy barrier ΔE in order to escape and be collected. There is likely a distribution of QD sizes, with a corresponding distribution E_{md} and ΔE. Smaller dots with smaller E_{md} that lead to the longer extended wavelength would need a larger activation energy ΔE for the photogenerated hole to escape; this is associated with a lower escape probability. This would explain why the extended cutoff response decreases as the wavelength increases.

Figure 17.11 also shows that the photoresponse increases with temperature; the responsivity at 225 K is approximately twice that at 125 K. Similar behavior is found in Fig. 17.12, which shows that the $T = 175$ K spectral QE under −0.1V, −0.2 V, and −0.5 V. It appears that ∼200-mV reverse bias is required for the photoresponse to fully turn on. In examining Figs. 17.11 and 17.12, we note that the ratio of the bulk InAsSb matrix response to the dot-to-matrix response stays approximately the same as the temperature or the applied bias increases. This indicates a common mechanism that blocks both types of photocurrent. One possible mechanism responsible for this behavior is the presence of a small unintended hB resulting from the valence-band mismatch between the absorber and the AlSbAs barrier (the valence-band edges of the absorber and the barrier should be aligned in an ideal nBn structure). This barrier would block photocurrents generated from both the InAsSb matrix absorption and the dot-to-matrix absorption.

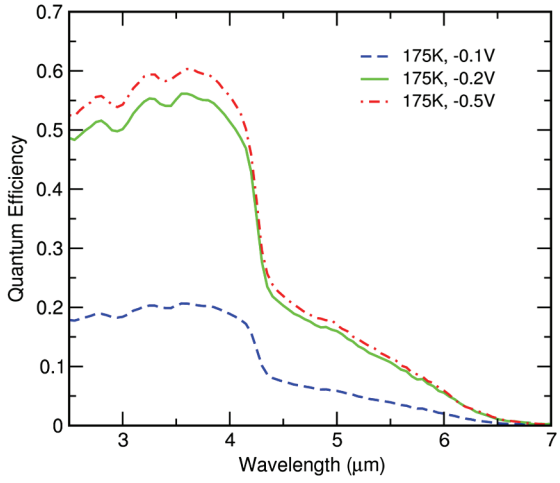

Figure 17.12 Double-pass spectral QE of a QD-BIRD structure under various applied biases, measured at 175 K. (See color plate section.)

A likely mechanism that explains the observed temperature and applied dependence of the spectral QE shown in Figs. 17.11 and 17.12 is the presence of a small unintended hB resulting from a valence-band offset ΔE_v between the absorber and the AlSbAs barrier (note that the valence-band edges of the absorber and the barrier should be aligned in an ideal nBn structure), as illustrated in Fig. 17.13. This barrier would block photocurrents generated from both the InAsSb matrix absorption and the dot-to-matrix absorption.

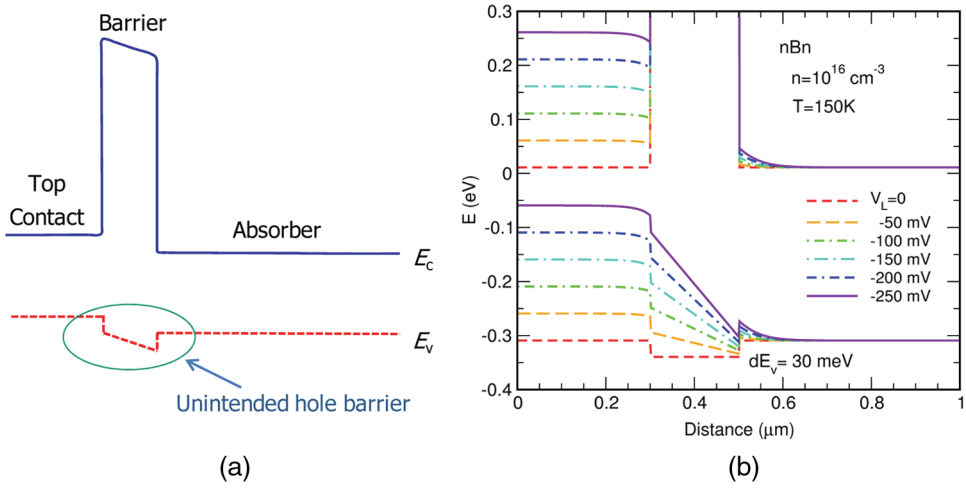

Figure 17.13 (a) Schematic illustration of a QD-BIRD structure with an unintended hole barrier. (b) Calculated energy band diagrams under various biasing conditions for a QD-BIRD structure with a 30-meV valence-band offset ΔE_v between the eB and the absorber. (See color plate section.)

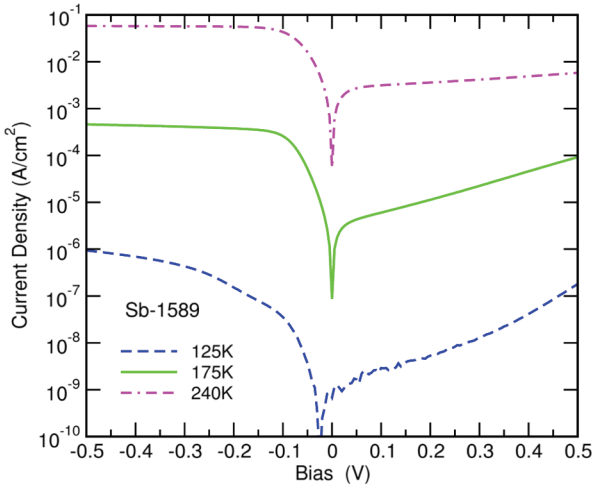

Figure 17.14 Dark-current density as a function of applied bias of a QD-BIRD taken at 125, 175, and 240 K. (See color plate section.)

Higher temperature could aid thermionic emission processes for climbing over the barrier, and applied bias could lower the barrier. We note that not all of the applied bias goes toward lowering the barrier; simulation results in Fig. 17.13 show that a barrier formed by a valence-band offset of $\Delta E_v =$ 30 meV would require ~200-mV reverse bias to overcome.

Figure 17.14 shows the measured dark-current density for a QD-BIRD as a function of applied bias at 125, 175, and 240 K. The reverse-bias (negative top contact bias) current–voltage characteristics appear diffusion limited at 175 and 240 K. Under −200-mV bias, the dark-current density levels are 1.52×10^{-7} A/cm^2 and 3.77×10^{-4} A/cm^2, respectively at 125 and 175 K. We computed the blackbody specific detectivity D^* for *f*/2 optics, in 300-K background conditions. The photocurrent is determined from the integrated photoresponse in the 3- to 6-μm spectral range. For a detector temperature of $T = 175$ K, under −200 mV bias, the blackbody D^* is dark-current limited and has a value of 1.07×10^{11} cm-Hz$^{1/2}$/W. At $T = 125$ K, the blackbody D^* becomes background limited and has a value of 3.76×10^{12} cm-Hz$^{1/2}$/W. Overall, the performance of the QD-BIRD is quite good. Optimization of the valence-band alignment between the absorber and the barrier should improve device characteristics. The bimodal photoresponse seems to be a basic property of this device architecture.

17.4 Summary

The antimonide material system is relatively robust and has the potential for good manufacturability. The versatility of the material system, with the availability of three different types of band offsets, provides great flexibility in device design. In the MWIR, the use of unipolar barriers in the nBn design has